CrystEngComm

ROYAL SOCIETY OF CHEMISTRY

PAPER

View Article Online
View Journal | View Issue

Cite this: *CrystEngComm*, 2025, **27**, 850

Crystal/magnetic structure and cation inversion in hydrothermally synthesized $MnFe_2O_4$, $CoFe_2O_4$, $NiFe_2O_4$, and $ZnFe_2O_4$ nanoparticles: a neutron powder diffraction study†

Henrik L. Andersen, *[a] Matilde Saura-Múzquiz, *[b] Cecilia Granados-Miralles, [c] Rebekka Klemmt, [d] Espen D. Bøjesen [d] and Mogens Christensen [e]

Received 1st October 2024,
Accepted 14th January 2025

DOI: 10.1039/d4ce01001a

rsc.li/crystengcomm

The crystal and magnetic structures of $MnFe_2O_4$, $CoFe_2O_4$, $NiFe_2O_4$ and $ZnFe_2O_4$ nanocrystallites are reported based on joint structural modelling of powder X-ray diffraction and neutron powder diffraction data. The nanoparticle samples were prepared using equivalent precursor preparation routes (co-precipitation of transition metal hydroxides using NH_4OH) and identical hydrothermal synthesis conditions (steel autoclave, 200 °C, 1 hour), allowing the isolated effect of the divalent cation to be evaluated. The study uncovers how variations in cation site preferences, spinel inversion degree, and crystallite size, which are challenging to discern using conventional characterization techniques, distinctly influence the magnetic structures. Diffraction peak profile analysis and scanning transmission electron microscopy images show how $MnFe_2O_4$ forms the largest crystallites (17.13(2) nm), followed by $NiFe_2O_4$ (10.31(1) nm) and $CoFe_2O_4$ (7.92(1) nm), while $ZnFe_2O_4$ forms ultrafine nanoparticles of only 3.70(1) nm. The transition metal ions have different affinities for the tetrahedral and octahedral crystallographic sites as evident from the obtained spinel inversion degrees, x, $[M^{2+}_{1-x}Fe^{3+}_{x}]^{tet}[M^{2+}_{x}Fe^{3+}_{2-x}]^{oct}O_4$. The $MnFe_2O_4$ and $CoFe_2O_4$ nanocrystallites exhibit mixed/semi-inverse spinel structures with x = 0.87(3) and 0.954(6), respectively, while $NiFe_2O_4$ is fully inverse (x = 1.00) and $ZnFe_2O_4$ is closer to a normal spinel (x = 0.138(4)). The combination of neutron diffraction and magnetic measurements illustrates how cation identity impacts site occupancy, crystallite size, and magnetization, providing new insights into the design of ferrite-based nanomaterials for magnetic applications.

Introduction

The spinel-structured ferrite compounds (MFe_2O_4, M = Mn, Fe, Co, Ni, Zn, *etc.*) are important magnetic materials, as their low cost, excellent resistance to corrosion and good magnetic performance make them crucial in a variety of applications, such as electromagnetic machinery (transformers/motors/generators), power supplies, high-frequency chokes and antennae, and microwave devices.[1] Furthermore, nanostructured spinel ferrite particles are currently being studied for uses in *e.g.* magnetic exchange-spring nanocomposites,[2,3] drug delivery,[4,5] neuromorphic spintronics,[6,7] magnetically recoverable nanocatalysts,[8,9] MRI contrast agents,[10,11] hyperthermia cancer treatment[12,13] and many more applications.[14] In all applications, the performance of the spinel ferrite particles can be optimized by tuning or maximizing their magnetic properties, which are directly determined by the complex interplay between the crystal-, magnetic-, and micro-structure of the nanoparticles.[15,16]

The spinel ferrites crystallize in the spinel structure (space group $Fd\bar{3}m$), which consists of a face centered cubic (fcc) lattice of cubic close packed oxygen atoms within which 1/8 of the tetrahedral sites and 1/2 of the octahedral sites are occupied by the transition metal ions (see Fig. 1). Notably, the different divalent cations can exhibit different affinities for the specific crystallographic sites resulting in formation of normal spinel structures (all M^{2+} occupying all tetrahedral 8*a* Wyckoff sites), inverse spinel structures (all M^{2+} occupying half the octahedral 16*d* Wyckoff sites) or mixed spinels with a fraction, x, of the Fe^{3+} ions (called the inversion degree) occupying the tetrahedral sites,

[a] *Instituto de Ciencia de Materiales de Madrid (ICMM), CSIC, 28049 Madrid, Spain. E-mail: henrik.andersen@csic.es*
[b] *Dept. de Física de Materiales, Universidad Complutense de Madrid, 28040 Madrid, Spain. E-mail: matsaura@ucm.es*
[c] *Instituto de Cerámica y Vidrio (ICV), CSIC, 28049 Madrid, Spain*
[d] *Interdisciplinary Nanoscience Center and Aarhus University Centre for Integrated Materials Research, Aarhus University, 8000 Aarhus C, Denmark*
[e] *Dept. of Chemistry and Interdisciplinary Nanoscience Center, Aarhus University, 8000 Aarhus C, Denmark*

† Electronic supplementary information (ESI) available. See DOI: https://doi.org/10.1039/d4ce01001a

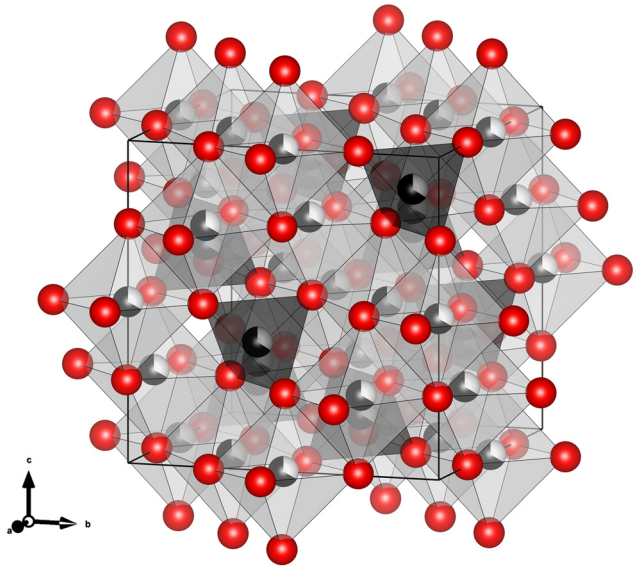

Fig. 1 Illustration of a mixed spinel structure in which both octahedral and tetrahedral sites are occupied by stoichiometric amounts of cations, *i.e.* 1/3 M^{2+} and 2/3 Fe^{3+}. Illustration made with VESTA.[26]

$[M^{2+}{}_{1-x}Fe^{3+}{}_{x}]^{tet}[M^{2+}{}_{x}Fe^{3+}{}_{2-x}]^{oct}O_4$. For larger/bulk crystallites, the thermodynamically stable cation distribution is normal in $ZnFe_2O_4$, mixed in $MnFe_2O_4$, and inverse in $CoFe_2O_4$ and $NiFe_2O_4$,[17] while nanosized crystallites have been reported to exhibit a variety of inversion degrees.[16,18–25]

The magnetic properties of spinel ferrites are closely linked to the type and distribution of cations between tetrahedral and octahedral sites, which determine the net magnetization and anisotropy. At room temperature, the spinel ferrite compositions mentioned above (except for the paramagnetic $ZnFe_2O_4$) display a ferrimagnetic ordering, which is governed by a relatively strong antiparallel super-exchange-coupling between the neighbouring ions on the tetrahedral and octahedral sites.[27] As there are twice as many octahedrally as tetrahedrally coordinated transition metal ions in the structure, the net magnetisation generally lies along the octahedral moment direction. Consequently, the intrinsic magnetic properties of MFe_2O_4 nanoparticles are determined by the choice of divalent cation, M^{2+}, and the distribution of the cationic species, M^{2+} and Fe^{3+}, between the crystallographic sites in the spinel structure. At room temperature, bulk $CoFe_2O_4$ is a hard magnet (first uniaxial magneto-crystalline anisotropy constant, K_1, of 290 kJ m^{-3} and saturation magnetisation, M_s, of 75 Am^2 kg^{-1}), $MnFe_2O_4$ and $NiFe_2O_4$ are soft magnets (M_s = 83 Am^2 kg^{-1} and 50 Am^2 kg^{-1}, respectively), and $ZnFe_2O_4$ is paramagnetic (antiferromagnet with Néel temperature, T_N, of 10 K).[27,28] Notably, we have previously demonstrated how hydrothermally synthesized $Zn_xCo_{1-x}Fe_2O_4$ ($0 \leq x \leq 1$) nanocrystallites can be trapped in a meta-stable mixed spinel cation configuration with higher saturation magnetisation compared to the thermodynamically stable bulk configuration.[29]

For nano-sized particles, variations in crystallite size can also have a particularly large influence on their magnetic behaviour, *i.e.* coercivity and susceptibility. In larger ferri-/ferromagnetic crystals, the build-up of magnetostatic energy in the structure drives a division of the crystal into distinct magnetic domains with different directions of magnetisation resulting in zero net magnetization.[27] These magnetic domains are separated by domain walls in which a gradual reorientation of the spins takes place across the domain wall thickness. When an external magnetic field is applied, the spin reorientation easily progresses in the material by gradual movement of magnetic domain walls. However, below a certain size threshold, domain formation is no longer energetically favourable compared to the magnetostatic energy of the uniformly magnetized body. Consequently, the crystallite can sustain a single magnetic domain and a coherent rotation of all spins is necessary to reverse the magnetisation of the crystallite. This leads to a substantial increase in the magnetic coercivity.[27] However, reducing the crystallite size further, below a certain limit, results in the particle entering a superparamagnetic state, in which a constant thermal flipping of the spins takes place, resulting in a loss of long-range magnetic order. In addition, very small nanoparticles have a considerable fraction of the magnetic atoms situated in the surface region where defects and dangling bonds cause their net magnetic moment to be reduced.[30,31] Consequently, the atomic- and nano-structural features discussed above directly determine the magnetic performance, *i.e.* coercive field, Curie/Neél temperature and saturation magnetisation of the materials.[17] In this context, understanding and controlling the relationship between spinel ferrite synthesis, nanocrystallite size, crystal structure and magnetic properties is key to optimizing their performance.

In the present study, the crystal and magnetic structures of hydrothermally synthesized nanosized spinel ferrite crystallites with compositions $MnFe_2O_4$, $CoFe_2O_4$, $NiFe_2O_4$ and $ZnFe_2O_4$, are determined and compared. The selected ferrites represent a range of spinel systems with distinct cation distributions and magnetic behaviors, enabling a systematic evaluation of how divalent cations influence structural and magnetic properties. These compositions also span typical bulk spinel configurations from normal to inverse, making them ideal candidates for studying how cation site preferences affect nanoscale magnetic properties. To isolate the effect of the individual divalent ions on the obtained crystallite size and structure, the samples were prepared using the same precursor preparation procedures (co-precipitation of transition metal hydroxides), and applying identical hydrothermal reaction conditions (steel autoclave, 200 °C, 1 hour) for all four compositions. Notably, this is made possible by using 25% NH_4OH, a relatively weak precipitating base (compared to the 12–16 M NaOH from our previous studies), since Mn oxidation and hematite (α-Fe_2O_3) impurity formation are known to occur in $MnFe_2O_4$ synthesis at high pH.[32] The structural analysis is carried out by joint Rietveld refinement of powder X-ray diffraction (PXRD) and

neutron powder diffraction (NPD) data. Here, the NPD technique is particularly advantageous as the scattering length of neutrons varies erratically with atomic number, giving much higher contrast between neighbouring elements in the periodic table than provided from conventional X-ray diffraction.[33] The magnetic structures of the ferrites are evaluated by implementation of a magnetic structural model in the NPD data refinements and related to the macroscopic magnetic properties observed using vibrating sample magnetometry (VSM).

Experimental

Sample preparation

Precursor preparation route. An aqueous 0.6 M iron(III) hydroxide dispersion was prepared by dropwise addition of 25% NH_4OH to a solution of $FeCl_3{\cdot}6H_2O$ (Sigma-Aldrich, ≥98% purity) under constant magnetic stirring until a pH of 10 was reached. The FeOOH dispersion was repeatedly washed with demineralized water, centrifuged (3 minutes, 2000 rpm) and decanted until the supernatant pH was under 8. Subsequently, the prepared 0.6 M FeOOH dispersion was mixed with 2.0 M aqueous MCl_2 solution (M = Mn, Co, Ni, or Zn depending on the desired product) in the desired nominal molar amount. Then, 25% NH_4OH was added dropwise under constant magnetic stirring until a pH of 10 was reached. Under these moderately alkaline aqueous conditions, Fe precipitates as the trivalent oxyhydroxide (FeOOH) while Mn, Co, Ni and Zn form divalent hydroxides ($M(OH)_2$).[34,35] Notably, particular care was taken in the case of Mn to not increase pH above 10, as it forms trivalent $Mn(OH)_3$ or may precipitate as mixed valence Mn_3O_4 under highly alkaline conditions.[34,36]

Autoclave synthesis. Gram-scale preparation of powders for neutron powder diffraction was carried out using 180 ml Teflon lined steel autoclaves as the reaction vessels, loaded with approximately 70 ml precursor. The autoclaves were placed in a convection oven preheated to 200 °C for 1 h. After the synthesis, the autoclaves were taken out of the oven and allowed to cool down at ambient temperature. Subsequently, the aqueous nanoparticle suspensions were washed with demineralized water and separated from the supernatant by centrifuging (3 minutes, 2000 rpm). The washing was repeated three times before the product was left to dry at 60 °C in a vacuum oven for >24 hours.

Characterisation

Laboratory PXRD. In-house powder X-ray diffraction patterns of the samples were collected at room temperature using a Rigaku SmartLab diffractometer (Rigaku, Japan) configured with cross beam optics in Bragg–Brentano geometry and equipped with a DteX/Ultra detector. The instrument was equipped with a cobalt anode (λ_1 = 1.7892 Å, λ_2 = 1.7931 Å). Data were collected in a 2θ-range of 15° to 125° ($Q_{max} \approx 6.2$ Å^{-1}) with an angular resolution of 0.021°.

Neutron powder diffraction. Neutron powder diffraction experiments were carried out at the Cold Neutron Powder Diffractometer (DMC) instrument at the Swiss Spallation Neutron Source (SINQ), Paul Scherrer Institute (PSI), Villigen, Switzerland at room temperature using a wavelength of 2.459 Å.[37] Data collection was carried out on approximately 2 g of powder loaded into a vanadium can. The DMC instrument is equipped with a linear position sensitive BF_3 multidetector consisting of 400 detector channels at an angular separation of 0.21° covering a total angular range of 79.81° ($Q_{max} \approx 3.7$ Å^{-1}). The detector was moved between two positions to attain an angular resolution of 0.11°.

Co-refinement of PXRD and NPD data. Co-refinement of PXRD and NPD data using a constrained structural model was carried out using the *Fullprof Suite* software package.[38] The model was based on the spinel structures of the given MFe_2O_4 (M = Mn, Co, Ni, Zn) composition in the cubic $Fd\bar{3}m$ space group. Linear restraints were imposed to avoid unphysical over- or under-population on the tetrahedral 8*a* and octahedral 16*d* Wyckoff sites while keeping a nominal stoichiometric ratio of 1 : 2 between M^{2+} and Fe^{3+}. The lattice parameters, crystallite size, atomic position of oxygen on the 32*e* Wyckoff site and an overall isotropic atomic displacement parameter (B_{iso}) were refined in a constrained manner, while scale factor, zero shift (or sample displacement in the case of the NPD) and background (Chebyshev polynomial) were refined for the individual patterns. The peak profiles were modelled using the Thompson–Cox–Hastings formulation of the pseudo-Voigt function.[39] The instrumental contribution to the peak profiles were determined by Rietveld refinement of data from a NIST LaB_6 660B line profile standard (PXRD) and a $Na_2Ca_3Al_2F_{14}$ standard (NPD), measured in the same instrumental configurations as the samples, and deconvoluted from the data in the refinements. The crystallite sizes (*i.e.* mean volume-averaged isotropic dimensions of coherently scattering crystalline domains), $\langle D \rangle$, were estimated from the refined peak broadening parameters by the Scherrer equation, $\langle D \rangle = (K{\cdot}\lambda)/(H{\cdot}\cos(\theta))$,[40] where λ is the wavelength, θ is the Bragg angle, H is the full width at half the maximum intensity, and K is the shape factor (here set to 0.829 assuming isotropic crystallite morphology).[41]

Magnetic structure refinement. For the NPD data, the contribution from the magnetic scattering was described using a collinear ferrimagnetic model with antiparallel magnetic moments on the tetrahedral and octahedral sites.[15] Notably, the magnetic easy axis in a cubic lattice is determined by the composition- and temperature-dependent magnetocrystalline anisotropy of the specific material. The magnetic easy axis of a cubic structure is along the ⟨100⟩ direction for materials with a positive first anisotropy constant ($K_1 > 0$), and along the ⟨111⟩ direction for materials with a negative first anisotropy constant ($K_1 < 0$).[17] Therefore, $CoFe_2O_4$ (K_1 = 290 kJ m^{-3}) at room temperature has its easy magnetization axis along ⟨100⟩, while the easy axes of $MnFe_2O_4$ (K_1 = −3 kJ m^{-3}) and $NiFe_2O_4$ (K_1 = −7 kJ

m^{-3}) lie along the ⟨111⟩ crystallographic direction.[27,28] However, the symmetry of cubic structures prevents discrimination between the different axis options by structural refinement of powder neutron diffraction data,[42] *i.e.* changing the direction of the refined Cartesian magnetic moment components, between ⟨100⟩ and ⟨111⟩ produces no difference in the obtained fit quality and refined magnetic moment magnitudes. Consequently, the theoretical magnetic easy axes, *i.e.* ⟨100⟩ for $CoFe_2O_4$ and ⟨111⟩ for $MnFe_2O_4$ and $NiFe_2O_4$, were employed in the refinements, with the ⟨111⟩ axis also being employed for the magnetic modelling of $ZnFe_2O_4$ (paramagnetic in theory) data.

STEM and STEM-EDS. The nanoparticles were suspended in pure (99.9%) ethanol and sonicated for ~4 min before they were drop-casted onto an Au 300 mesh grid with an ultrathin (approx. 3 nm) carbon film on lacey carbon. Scanning transmission electron microscopy (STEM) images and STEM energy-dispersive X-ray spectroscopy (EDS) datasets were collected using a Talos FX-200 operated at an acceleration voltage of 200 keV. The beam convergence angle was 10.5 mrad. The collection angle of the high angle annular dark field (HAADF) detector was 60–200 mrad. STEM-EDS data was collected using the installed Bruker ChemiSTEM system. The total collection time of each EDS dataset differed between ~3

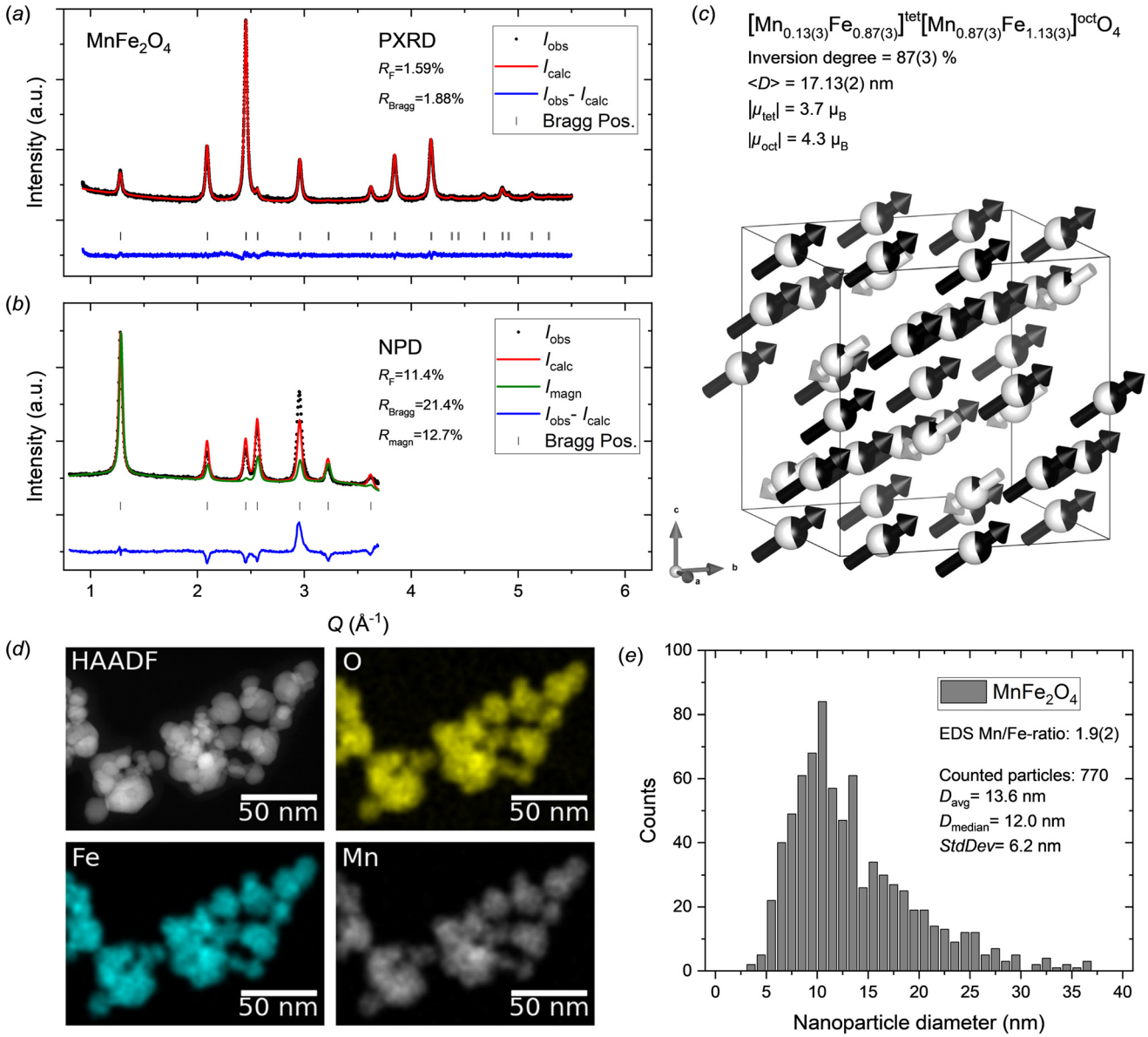

Fig. 2 a) PXRD and b) NPD data for $MnFe_2O_4$ nanocrystallites with jointly refined Rietveld fits. c) Illustration of the refined crystal and magnetic structure of the $MnFe_2O_4$ sample. The white and black arrows indicate the relative magnitudes and orientations of the refined magnetic moment components on tetrahedral and octahedral sites, respectively. The refined atomic site occupation fractions of Mn^{2+} (black) and Fe^{3+} (white) are illustrated on the spheres. Illustration made with VESTA.[26] d) STEM-HAADF image and EDS elemental maps for the $MnFe_2O_4$ nanoparticle sample. e) $MnFe_2O_4$ nanoparticle size analysis from STEM data.

min and ~25 min depending on a trade-off between optimizing signal-to-noise and minimizing contamination build-up. The latter was quite significant for the $ZnFe_2O_4$ sample, which made long data collection times impossible.

Size distributions were determined manually using the software FIJI.[43] It was assumed that the particles were spherical. Between 165 and 770 particles were counted for the four different samples. The STEM images were plotted using the python libraries HyperSpy,[44] Pandas,[45] numpy,[46] and Matplotlib.[47]

For the analysis of the EDS dataset, the automated quantification of the atomic fraction implemented to the Velox software used to control the ChemiSTEM system was used to obtain the averaged atomic ratios between the elements, no absorption correction was used. The EDS element maps were plotted using the python library HyperSpy.[44] For this, the background around the relevant elemental peaks were subtracted using a linear background interpolation prior to integration over the elemental peak, as implemented in HyperSpy.[44] The individual count maps were smoothed using a Gaussian kernel of 1 pixel and plotted using the python libraries SciPy,[48] and Matplotlib.[47]

Magnetic properties. Magnetic hysteresis curves were measured using a Quantum Design Physical Property Measurement System (PPMS) equipped with a Vibrating Sample Magnetometer (VSM). The field dependent magnetisation of the samples was measured at 300 K on cold pressed pellets (diameter = 2.7 mm, mass = 5–20 mg) by scanning the external field between ±1592 kA m^{-1} (±2 T). The measurements were conducted at a frequency of 40 Hz and an averaging time of 2 seconds.

Results and discussion

Crystal-, magnetic- and microstructure of $MnFe_2O_4$ nanocrystallites

Fig. 2a and b show the PXRD and NPD data with Rietveld refined fits obtained from the $MnFe_2O_4$ nanoparticle sample. The diffraction patterns show no indication of any secondary crystalline phases, as all reflections can be attributed to the spinel ferrite structure. The refined atomic structure is illustrated in Fig. 2c and the structural parameters are summarized in Table 1. A relatively good fit is obtained for the PXRD data; however, the model struggles to fully describe the NPD data. In particular, the (400) Bragg reflection at $Q \approx 3$ Å^{-1} in the NPD data, which has a significant contribution from both the nuclear and magnetic scattering, shows a considerable misfit. Since, Mn^{2+} and Fe^{3+} have the same electron configuration ($3d^5$), and therefore very similar X-ray scattering form factors,[49] their respective content and position in the structure cannot be accurately determined from PXRD data alone, as equivalent PXRD fit quality will be obtained irrespective of cation distribution.[50] Thus, the obtained distribution of cations relies on the fit to the NPD data, which for the $MnFe_2O_4$ sample studied here exhibits a considerable contribution from the magnetic structure. Considering that the misfit is mainly observed for the NPD data, the cause can be several factors including: 1) incorrect cation distribution between tetrahedral (8*a*) and octahedral (16*d*) sites; 2) incorrect assumption of stoichiometric sample composition, *i.e.* Mn/Fe ratio erroneously fixed in the refinement; 3) oxidation of Mn^{2+} to Mn^{3+} and introduction of cation vacancies in the spinel structure (similar to the ambiguous cases in the maghemite (γ-Fe_2O_3) and magnetite (Fe_3O_4) systems);[51] 4) incorrect or oversimplified model for the magnetic structure, which is assumed to be isostructural to the nuclear structure (same unit cell), with antiparallel moments on the 8*a* and 16*d* site aligned along the ⟨111⟩ crystallographic direction.

To evaluate these potential causes, various changes to the structural model were tested (see Supporting Information). Notably, free refinement of cation occupancies (Mn^{2+}, Mn^{3+}, Fe^{2+}, Fe^{3+}) and vacancy concentrations on the tetrahedral and octahedral sites is impossible due to heavy correlations leading to refinement divergence. Thus, a stable refinement can only be achieved by implementing linear restraints on composition and

Table 1 Atomic structure parameters for the $MnFe_2O_4$ nanocrystallite sample

$MnFe_2O_4$							
Space group: $Fd\bar{3}m$ (#227)							
Unit cell: $a = b = c = 8.49637(9)$ Å, $\alpha = b = \gamma = 90°$							
Fit quality PXRD: $R_{Bragg} = 1.88\%$, $R_F = 1.59\%$							
Fit quality NPD: $R_{Bragg} = 21.4\%$, $R_F = 11.4\%$, $R_{magn} = 12.7\%$							
Atom	Wyckoff site	*x*	*y*	*z*	B_{iso} (Å^2)	*sof*[a]	R_x[b] (μ_B)
Mn	8*a*	0.125	0.125	0.125	1.24(1)[c]	0.13(3)[d]	−2.1
Fe	8*a*	0.125	0.125	0.125	1.24(1)[c]	0.87(3)[d]	−2.1
Mn	16*d*	0.5	0.5	0.5	1.24(1)[c]	0.44(2)[d]	2.5
Fe	16*d*	0.5	0.5	0.5	1.24(1)[c]	0.56(2)[d]	2.5
O	32*e*	0.25695(9)	0.25695(9)	0.25695(9)	1.24(1)[c]	1	0

Note: the numbers in parentheses indicate the errors on the last significant digit of the refined parameters. [a] Site occupation fraction (*sof*). [b] The magnetic moment vector component ($R_x = R_y = R_z$) refined along the ⟨111⟩ direction. [c] The atomic displacement parameters (B_{iso}) were constrained to be equal. [d] Linear restraints were imposed on the tetrahedral (8*a*) and octahedral (16*d*) site occupancies to avoid unphysical over-population and constrain to nominal composition.

site occupancies (as described in the experimental section) or fixing certain parameters. The tested models include: 1) free refinement of Mn-content (site occupation fractions linearly restrained to 1.0). 2) Magnetite, *i.e.* Mn-deficient structure (Fe_3O_4). 3) Maghemite, *i.e.* Mn-deficient structure with disordered vacancies (γ-Fe_2O_3). 4) Maghemite-like structure with disordered vacancies and nominal stoichiometric Mn : Fe ratio (γ-$Mn_{0.67}Fe_{1.33}O_3$). 5) Changing from divalent to trivalent Mn in the magnetic structure. However, significantly poorer fits were obtained for options 1–4 and option 5 yielded no noticeable improvement compared to the initially employed $MnFe_2O_4$ model (see ESI†). Notably, STEM-EDS maps (see Fig. 2d) show a homogeneous elemental distribution in the $MnFe_2O_4$ nanoparticles confirming the single-phase nature of the sample, and the 1 : 2 metal ion stoichiometry was confirmed by quantitative analysis of EDS spectra. Furthermore, in a previous study, we employed X-ray absorption spectroscopy (XAS) to confirm the oxidation states in spinel ferrite nanoparticles, including analogously prepared $MnFe_2O_4$ nanocrystallites, which confirmed divalent Mn and trivalent Fe.[15] In addition, the refined cell parameter of 8.49637(9) Å is in good agreement with previous reports for stoichiometric $MnFe_2O_4$ (typically ~8.5 Å)[52,53] rather than those generally reported for Fe_3O_4 or γ-Fe_2O_3 (typically ~8.35–8.40 Å),[18,54,55] indicating that the assumptions of nominal $MnFe_2O_4$ composition in the sample, Mn^{2+} and Fe^{3+} oxidation states and no vacancies in the structure are likely correct. Consequently, despite the shortcoming of the employed model, the cause for the misfit could not be identified, and no better description could be achieved here.

The peak profile analysis yielded a mean $MnFe_2O_4$ crystallite dimension, $\langle D \rangle$, of 17.13(2) nm. The atomic structure refinement yielded an inversion degree of 87(3)%, which is significantly different from the value for bulk $MnFe_2O_4$, which is generally reported to have around 20–25% inversion.[56,57] However, disordered cation distributions (inversion degrees of ~60–70%, *i.e.* near-stoichiometric and disordered Mn/Fe occupancy on each site) have previously been reported for fine nanocrystallites (<10 nm).[18,19]

The contribution from magnetic scattering to the NPD data was modelled by implementing a collinear ferrimagnetic structure with antiparallel moments on the 8*a* and 16*d* site aligned along the ⟨111⟩ crystallographic direction. Concurrent and unconstrained refinement of the Mn^{2+} and Fe^{3+} Cartesian magnetic moment components on both tetrahedral and octahedral sites (together with site occupancies) introduced too many degrees of freedom and excessive parameter correlations, thereby causing refinement divergence. Consequently, the magnetic orientations were fixed to lie along the ⟨111⟩ direction (*i.e.* $R_x = R_y = R_z$ constraint) and average moments (*i.e.* $R_{Mn} = R_{Fe}$ constraint) were refined for each of the tetrahedral and octahedral sites, yielding net magnetic moments, $\mu = (R_x^2 + R_y^2 + R_z^2)^{1/2}$, of $|\mu_{tet}| = 3.7\mu_B$ and $|\mu_{oct}| = 4.3\mu_B$.

As mentioned earlier, the STEM-EDS maps show a homogeneous elemental distribution in the $MnFe_2O_4$ nanoparticles (see Fig. 2d) and EDS spectra collected in several different regions yielded an average Mn/Fe ratio of 1.9(2), which agrees with the formal 1 : 2 ratio. The STEM images (see Fig. 2d and ESI†) confirm the nanocrystalline nature and isotropic morphology of the nanoparticles. Particle size analysis was carried out by manual measurement of 770 individual particles across representative STEM micrographs taken different places on the grids. The resulting particle size distribution is shown in Fig. 2e. The obtained average particle size of 13.6 ± 6.2 nm, although somewhat smaller, is compatible with the crystallite size from the diffraction data analysis (17.13(2) nm). The discrepancy can be ascribed to the relatively broad and skewed lognormal-like size distribution, which enhances the difference between the average number weighted size from STEM analysis and volume-weighted size that is inherently obtained from diffraction data.

Crystal-, magnetic- and microstructure of $CoFe_2O_4$ nanocrystallites

Fig. 3a and b show the PXRD and NPD patterns and corresponding jointly refined Rietveld fits for the hydrothermally synthesized $CoFe_2O_4$ nanocrystallite sample. All reflections could be attributed to the spinel ferrite structure and the data show no indication of any secondary crystalline phases. Relatively good fits were obtained to both the PXRD and NPD data, however, like the $MnFe_2O_4$ sample discussed above, a considerable misfit is observed for the (400) reflection at ~3 $Å^{-1}$. The refined atomic and magnetic structure is shown in Fig. 3c and the structural parameters are provided in Table 2. The obtained cell parameter of 8.3901(1) Å is in good agreement with previously reported values for $CoFe_2O_4$ nanocrystallites, further supporting that nominal stoichiometry and phase purity have been achieved.[15,18,58,59] The peak profile analysis yields a mean crystallite size of 7.92(1) nm and the atomic structure refinement indicates an almost fully inverse spinel structure with an inversion degree of 95.4(6)%. This value is in agreement with the known bulk preference for the inverse configuration,[17] although nanosized $CoFe_2O_4$ crystallites have been reported to adopt mixed spinel structures.[18,59] This could indicate a size- and/or synthesis method-dependent nature of the cation configuration in $CoFe_2O_4$. The collinear ferrimagnetic structure was refined along the ⟨100⟩ crystallographic direction given the hard magnetic properties of the compound (see experimental section), with net magnetic moments of 3.5 and 3.6μ_B obtained for the tetrahedral and octahedral sites, respectively.

The elemental mapping by STEM-EDS shows a homogeneous distribution of the metal ions in the $CoFe_2O_4$ nanoparticles (see Fig. 3d), which is consistent with a single-phase sample. Quantitative analysis of EDS spectra collected in several different regions yielded an average Co/Fe ratio of 2.2(3), which agrees well with the formal 1 : 2 metal ion stoichiometry. The nanocrystalline nature and isotropic morphology of the nanoparticles were confirmed by the STEM images (see Fig. 3d and ESI†). Particle size analysis

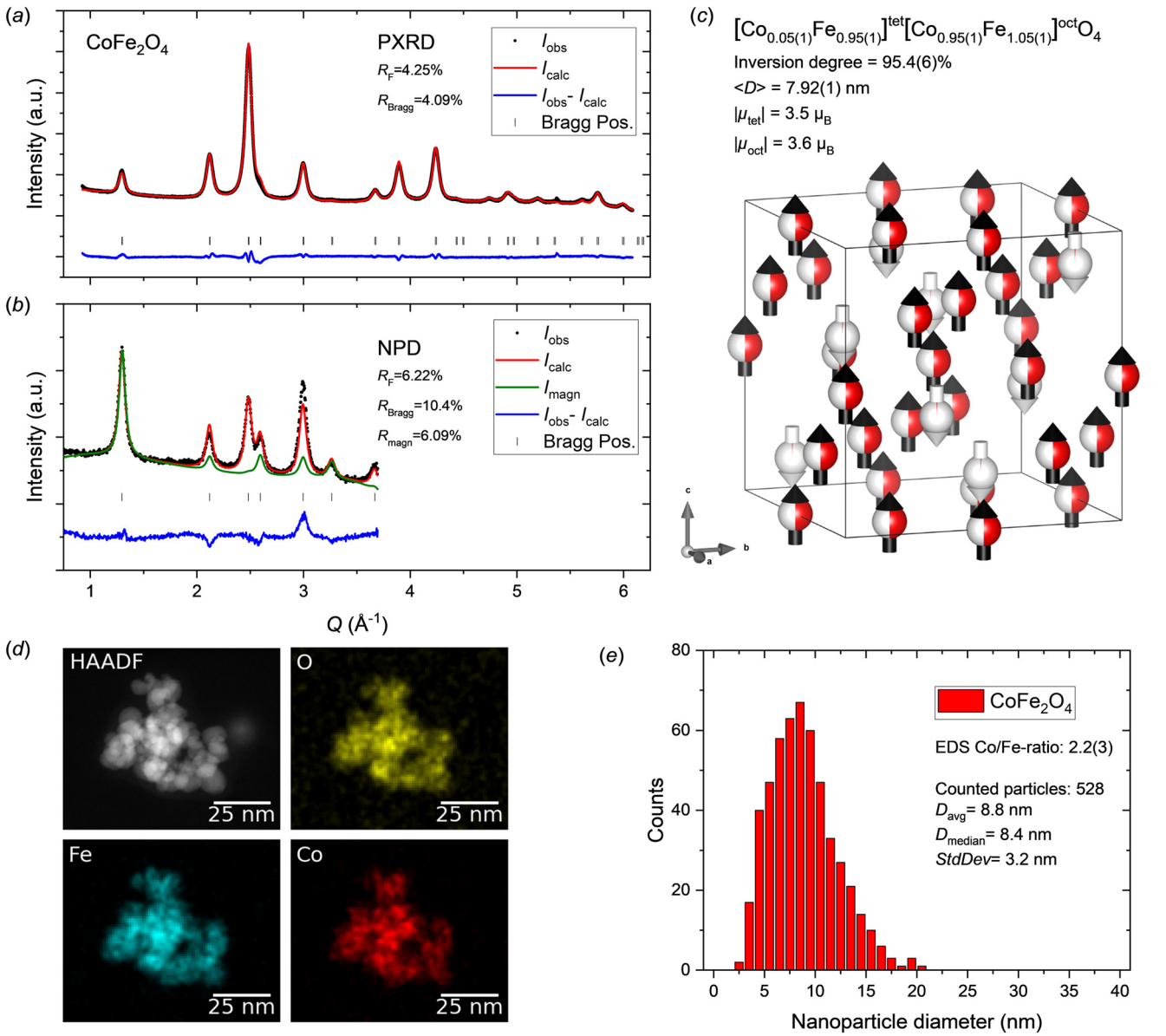

Fig. 3 a) PXRD and b) NPD data for $CoFe_2O_4$ nanocrystallites with jointly refined Rietveld fits. c) Illustration of the refined crystal and magnetic structure of the $CoFe_2O_4$ sample. The white and black arrows indicate the relative magnitudes and orientations of the refined magnetic moment components on tetrahedral and octahedral sites, respectively. The refined atomic site occupation fractions of Co^{2+} (red) and Fe^{3+} (white) are illustrated on the spheres. Illustration made with VESTA.[26] d) STEM-HAADF image and EDS elemental maps for the $CoFe_2O_4$ nanoparticle sample. e) $CoFe_2O_4$ nanoparticle size analysis from STEM data.

was carried out by manual measurement of 528 individual particles across representative STEM micrographs taken different places on the grids. The resulting particle size distribution is shown in Fig. 3e. The average particle size of 8.8 ± 3.2 nm agrees well with the nanocrystallite size obtained from the diffraction data analysis (7.92(1) nm).

Crystal-, magnetic- and microstructure of $NiFe_2O_4$ nanocrystallites

Fig. 4a and b show the jointly refined PXRD and NPD patterns collected on the $NiFe_2O_4$ nanocrystallites. The diffraction data show no indications of secondary crystalline phases and relatively good fits were obtained for both the PXRD and NPD patterns, including the (400) peak of the NPD data, which was not fully described for the $MnFe_2O_4$ and $CoFe_2O_4$ samples. The refined crystal- and magnetic structure is illustrated in Fig. 4c and the structural parameters are provided in Table 3. A cubic cell parameter of 8.3574(1) Å was obtained, which is in good agreement with previously reported values for $NiFe_2O_4$ (~8.33–8.36 Å).[60–63] In the bulk, $NiFe_2O_4$ is an inverse spinel,[17] however, both inverse and mixed spinel structures have been reported for nanosized crystallites,[18,20–22] indicating a potential dependence on

Table 2 Atomic structure parameters for the $CoFe_2O_4$ nanocrystallite sample

$CoFe_2O_4$							
Space group: $Fd\bar{3}m$ (#227)							
Unit cell: $a = b = c = 8.3901(1)$ Å, $\alpha = b = \gamma = 90°$							
Fit quality PXRD: $R_{Bragg} = 4.09\%$, $R_F = 4.25\%$							
Fit quality NPD: $R_{Bragg} = 10.4\%$, $R_F = 6.22\%$, $R_{magn} = 6.09\%$							
Atom	Wyckoff site	x	y	z	B_{iso} (Å^2)	sof[a]	R_x[b] (μ_B)
Co	8*a*	0.125	0.125	0.125	1.09(1)[c]	0.046(6)[d]	−3.5
Fe	8*a*	0.125	0.125	0.125	1.09(1)[c]	0.954(6)[d]	−3.5
Co	16*d*	0.5	0.5	0.5	1.09(1)[c]	0.477(3)[d]	3.6
Fe	16*d*	0.5	0.5	0.5	1.09(1)[c]	0.523(3)[d]	3.6
O	32*e*	0.25634(8)	0.25634(8)	0.25634(8)	1.09(1)[c]	1	0

Note: the numbers in parentheses indicate the errors on the last significant digit of the refined parameters. [a] Site occupation fraction (*sof*). [b] The magnetic moment vector component (R_x) refined along the ⟨100⟩ direction. [c] The atomic displacement parameters (B_{iso}) were constrained to be equal. [d] Linear restraints were imposed on the tetrahedral (8*a*) and octahedral (16*d*) site occupancies to avoid unphysical over-population and constrain to nominal composition.

particle size or synthesize route. Here, the initial linearly restrained refinement of the site occupancies led to a slight unphysical overpopulation of Ni^{2+} on the 16*d* site and under population on the 8*a* site, indicating a strong preference for the inverse spinel configuration. Therefore, the site occupations were fixed to the fully inverse distribution in the final refinement. The peak profile analysis yielded a mean crystallite size of 10.31(1) nm. Given that $NiFe_2O_4$ is a soft magnetic material, the atomic magnetic moment components were refined along the theoretically preferred space diagonal of the cubic unit cell (⟨111⟩ direction). Net moments of 3.6 and 3.1μ_B were obtained for the 8*a* and 16*d* sites, respectively.

The STEM-EDS maps of the $NiFe_2O_4$ nanoparticles show an even homogeneous distribution of Ni and Fe in the sample (see Fig. 4d) corroborating the single-phase nature. The 1 : 2 metal ion stoichiometry of the Ni spinel ferrite compound was confirmed by quantitative analysis of EDS spectra collected in several different regions yielding an average Ni/Fe ratio of 2.1(2). The STEM images (see Fig. 4d and ESI†) confirm the nanocrystalline nature and isotropic morphology of the nanoparticles. Particle size analysis was carried out by manual measurement of 394 individual particles across representative TEM micrographs taken different places on the grids. The resulting particle size distribution is shown in Fig. 4e. The obtained average particle size of 9.4 ± 3.2 nm is agreement with crystallite dimension from the diffraction data analysis (10.31(1) nm).

Crystal-, magnetic- and microstructure of $ZnFe_2O_4$ nanocrystallites

The PXRD and NPD patterns of the $ZnFe_2O_4$ nanocrystallite sample and the corresponding Rietveld fits are shown in Fig. 5a and b. As evident from the highly broadened diffraction peaks, the $ZnFe_2O_4$ sample consists of ultrafine crystallites ($\langle D \rangle$ = 3.70(1) nm). The diffraction data do not show any additional crystalline phases to be present in the sample as all peaks are well described by the spinel structure model. The refined crystal- and magnetic structure is illustrated in Fig. 5c and the structural parameters are provided in Table 4. A cell parameter of 8.4588(4) is obtained, which agrees with the relatively large variety of previously reported values for $ZnFe_2O_4$ nanoparticles (~8.39–8.45 Å), when considering the very small particles size, which often causes some cell expansion due to the increased surface/bulk ratio.[18,23,64,65] A spinel inversion of 13.8(4)% is obtained from the refinement, which differs from the thermodynamically stable normal spinel configuration,[17] but falls within the various degrees of inversion between 0 and 0.6 that have been reported for nanosized crystallites in the literature.[18,23,24] At first glance, the combination of an almost completely normal spinel structure, with the majority of non-magnetic Zn^{2+} on the tetrahedral site, could be expected to yield a highly optimized intrinsic magnetic performance. However, the very low amount of a magnetic species (Fe^{3+}) on the tetrahedral site leads to a destabilization of the magnetic structure due to the weak antiferromagnetic tetrahedral–octahedral superexchange coupling. This causes the material to be paramagnetic at room temperature (as evident from the magnetization data discussed later) and is the reason for the very weak magnetic scattering observed. At very low temperature (<10 K), $ZnFe_2O_4$ forms a long-range antiferromagnetic structure, as the low thermal energy allows extended antiferromagnetic superexchange coupling between the octahedral Fe^{3+} moments.[66] Here, despite the largely paramagnetic nature of the sample, the small magnetic scattering contribution was modelled based on a collinear ferrimagnetic structure along the ⟨111⟩ crystallographic direction, yielding small net moments of 1.9 and 1.5μ_B on the tetrahedral and octahedral sites, respectively. The small amount of long-range magnetic diffraction signal present can be ascribed to a slight magnetic ordering induced by the small amount of tetrahedral Fe^{3+}, which results in regions with sufficient coherently scattering magnetic ordering.

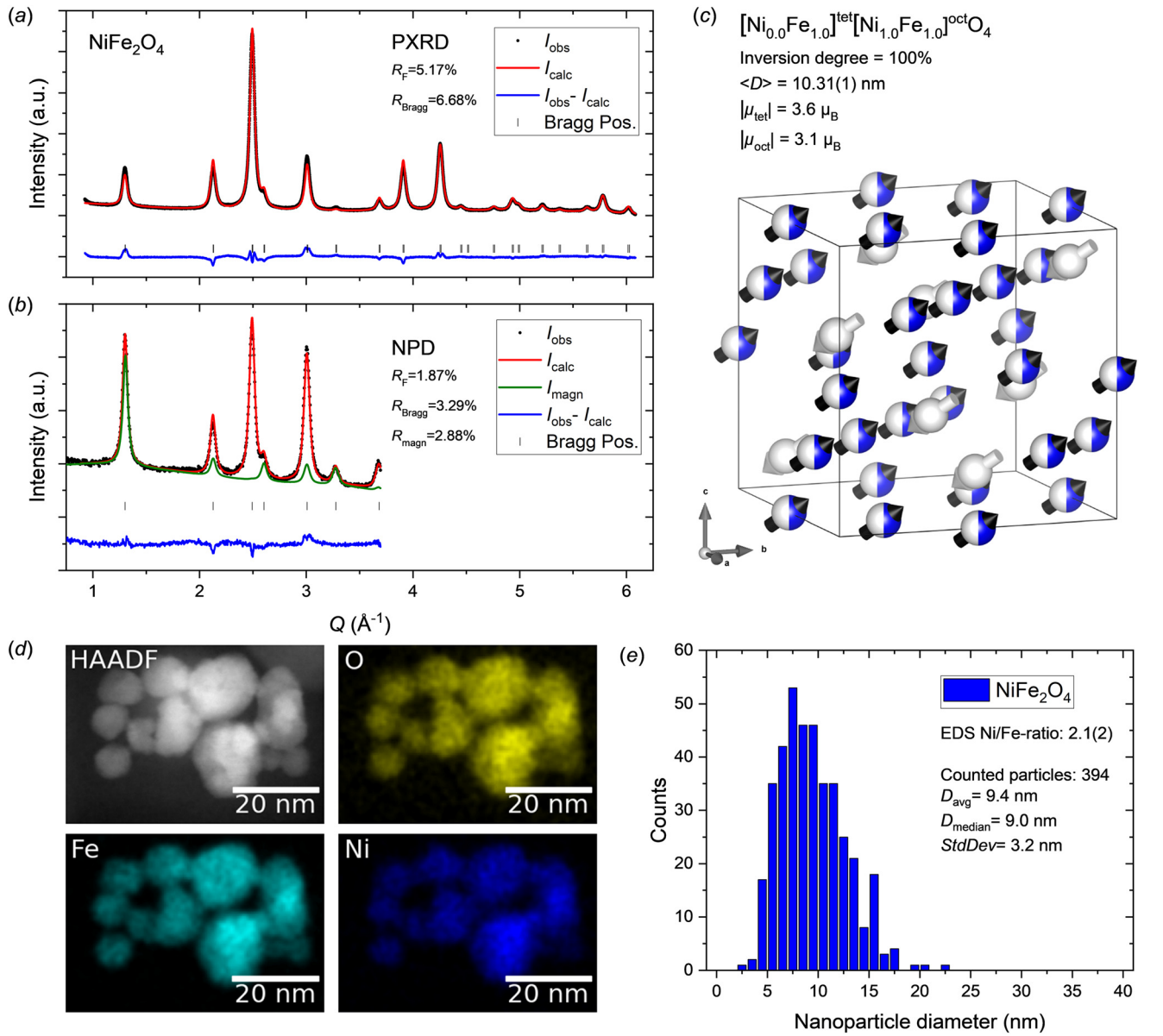

Fig. 4 a) PXRD and b) NPD data for $NiFe_2O_4$ nanocrystallites with jointly refined Rietveld fits. c) Illustration of the refined crystal and magnetic structure of the $NiFe_2O_4$ sample. The white and black arrows indicate the relative magnitudes and orientations of the refined magnetic moment components on tetrahedral and octahedral sites, respectively. The atomic site occupation fractions of Ni^{2+} (blue) and Fe^{3+} (white) are illustrated on the spheres. Illustration made with VESTA.[26] d) STEM-HAADF image and EDS elemental maps for the $NiFe_2O_4$ nanoparticle sample. e) $NiFe_2O_4$ nanoparticle size analysis from STEM data.

Fig. 5d shows a representative STEM-EDS map illustrating the homogeneous elemental distribution in the $ZnFe_2O_4$ nanoparticles. The expected 1 : 2 metal ion stoichiometry was confirmed by quantitative analysis of EDS spectra collected in several different regions yielding an average Zn/Fe ratio of 2.3(4). The nanocrystalline nature and isotropic morphology of the nanoparticles are confirmed by the TEM images (see Fig. 5d and ESI†). Particle size analysis was carried out by manual measurement of 165 individual particles across representative STEM micrographs taken different places on the grids. The resulting particle size distribution is shown in Fig. 5e. The obtained average particle size of 5.1 ± 1.6 nm is compatible with the crystallite size from the diffraction data analysis (3.70(1) nm).

Magnetic properties

The magnetic hysteresis curves of the four samples collected by VSM are shown in Fig. 6a, illustrating their distinct magnetic behaviour as a result of their different atomic- and nano-structural natures. The $MnFe_2O_4$ (M_s = 63.0(1) Am^2 kg^{-1}), $CoFe_2O_4$ (M_s = 64.2(1) Am^2 kg^{-1}) and $NiFe_2O_4$ (M_s = 50.2(1) Am^2 kg^{-1}) nanocrystallite samples exhibit magnetic responses characteristic of soft magnets, while the $ZnFe_2O_4$

Table 3 Atomic structure parameters for the $NiFe_2O_4$ nanocrystallite sample

$NiFe_2O_4$							
Space group: $Fd\bar{3}m$ (#227)							
Unit cell: $a = b = c = 8.3574(1)$ Å, $\alpha = b = \gamma = 90°$							
Fit quality PXRD: $R_{Bragg} = 6.68\%$, $R_F = 5.17\%$							
Fit quality NPD: $R_{Bragg} = 3.29\%$, $R_F = 1.87\%$, $R_{magn} = 2.88\%$							
Atom	Wyckoff site	x	y	z	B_{iso} (Å^2)	sof[a]	R_x[b] (μ_B)
Ni	8*a*	0.125	0.125	0.125	0.66(1)[c]	0	−2.1
Fe	8*a*	0.125	0.125	0.125	0.66(1)[c]	1	−2.1
Ni	16*d*	0.5	0.5	0.5	0.66(1)[c]	0.5	1.8
Fe	16*d*	0.5	0.5	0.5	0.66(1)[c]	0.5	1.8
O	32*e*	0.25841(9)	0.25841(9)	0.25841(9)	0.66(1)[c]	1	0

Note: the numbers in parentheses indicate the errors on the last significant digit of the refined parameters. [a] Site occupation fraction (*sof*). [b] The magnetic moment vector component ($R_x = R_y = R_z$) refined along the ⟨111⟩ direction. [c] The atomic displacement parameters (B_{iso}) were constrained to be equal.

(M_s = 6.1(1) Am^2 kg^{-1}) sample is paramagnetic. Notably, bulk $CoFe_2O_4$ is known to exhibit semi-hard magnetic properties with an effective magnetocrystalline anisostropy constant, K_1, of 290 kJ m^{-3} and a Curie temperature, T_C, of 790 °C.[27] Thus, the lack of a coercive field indicates that the dimensions of the synthesized $CoFe_2O_4$ particles are below the superparamagnetic limit. The spin reversal time, τ, for superparamagnetic nanoparticles can be estimated by the Néel–Brown law, $\tau = \tau_0 \exp(K_1V/k_BT)$, where τ_0 is the attempt time (~1 ns), k_B is the Boltzmann constant, V is the crystallite volume, and T is the temperature.[28,67] For isotropic crystallites, the critical superparamagnetic threshold diameter D_{sp} can be obtained from the Néel–Brown law as follows: $D_{sp} = [6k_BT\ln[\tau/\tau_0]/(\pi K_1)]^{1/3}$. By setting the spin reversal time equal to the VSM measurement averaging time (2 s), a critical dimension of ~8.4 nm is obtained for $CoFe_2O_4$ at 300 K. The average crystallite size of 7.92(1) nm obtained from peak profile analysis of the diffraction data is therefore below the superparamagnetic limit and in agreement with the observed lack of magnetic hysteresis. The slight opening of the hysteresis loop for the $CoFe_2O_4$ sample illustrated in the insert of Fig. 6a (H_c = 13.2(2) kA m^{-1}) can be attributed to polydispersity with a minor part of the crystallites having sizes above the critical dimension.

The magnetic properties of spinel ferrites depend on a combination of factors, including the type of divalent ion, the spinel inversion degree, and the crystallite size.[17] As demonstrated in our previous studies, the inversion degree of spinel ferrite nanoparticles may differ significantly from their bulk counterparts and may vary considerably depending on employed synthesis conditions and/or with thermal history.[15,29,68] Fig. 6b compares the saturation magnetizations calculated from the refinements of structure and magnetic moment in the NPD, M_{NPD}, to the observed macroscopic saturation magnetizations, M_s, from the VSM data. The M_{NPD} value may be used as an estimate for the upper-limit intrinsic saturation magnetization permitted by the structure for a fully crystalline sample. Although the magnetizations from the two methods follow similar trends, the plot also illustrates the somewhat limited agreement between the two approaches and the relatively poor predictive capability of the M_{NPD} value. This may be due to several factors, including the very high uncertainties of the magnetic structure refinement, reduced crystallinity of the sample, and the influence of microstructural and finite-size effects.[30,31]

Discussion

All of the ferrite samples studied here ($MnFe_2O_4$, $CoFe_2O_4$, $NiFe_2O_4$, and $ZnFe_2O_4$) were confirmed to be spinel structured, nanosized and phase pure (*i.e.* no crystalline impurities observed). To ensure the formation of phase-pure spinel ferrites without impurities such as hematite (α-Fe_2O_4) or manganese oxides, several key parameters were carefully controlled. A precise stoichiometry of the metal ions was maintained to match the target spinel compositions, ensuring a balanced cation distribution. Uniform mixing of the precursor species was achieved through constant magnetic stirring during the dropwise addition of 25% NH_4-OH, which provided a moderately basic environment (pH ≈ 10). This pH was critical for promoting the precipitation of homogeneous FeOOH and $M(OH)_2$ gels, especially for $MnFe_2O_4$, where excessive alkalinity could lead to manganese oxide impurities.[34,35] The presence of divalent transition metal species in the precursor mixture further ensured spinel phase formation, as highlighted by our earlier study showing their role in preventing α-Fe_2O_3 crystallization.[69]

The obtained crystallite sizes, unit cell lengths, cation inversion degrees and saturation magnetisations of the samples from this study are summarised in Table 5, where they are compared to values from our previous studies employing different precursor routes and/or synthesis conditions.[15,29] Variations in cell parameters (PXRD peak positions) and crystallite/particle size (PXRD peak widths and STEM analysis) caused by the distinct chemistries of the different divalent transition metal ions are observed. In the

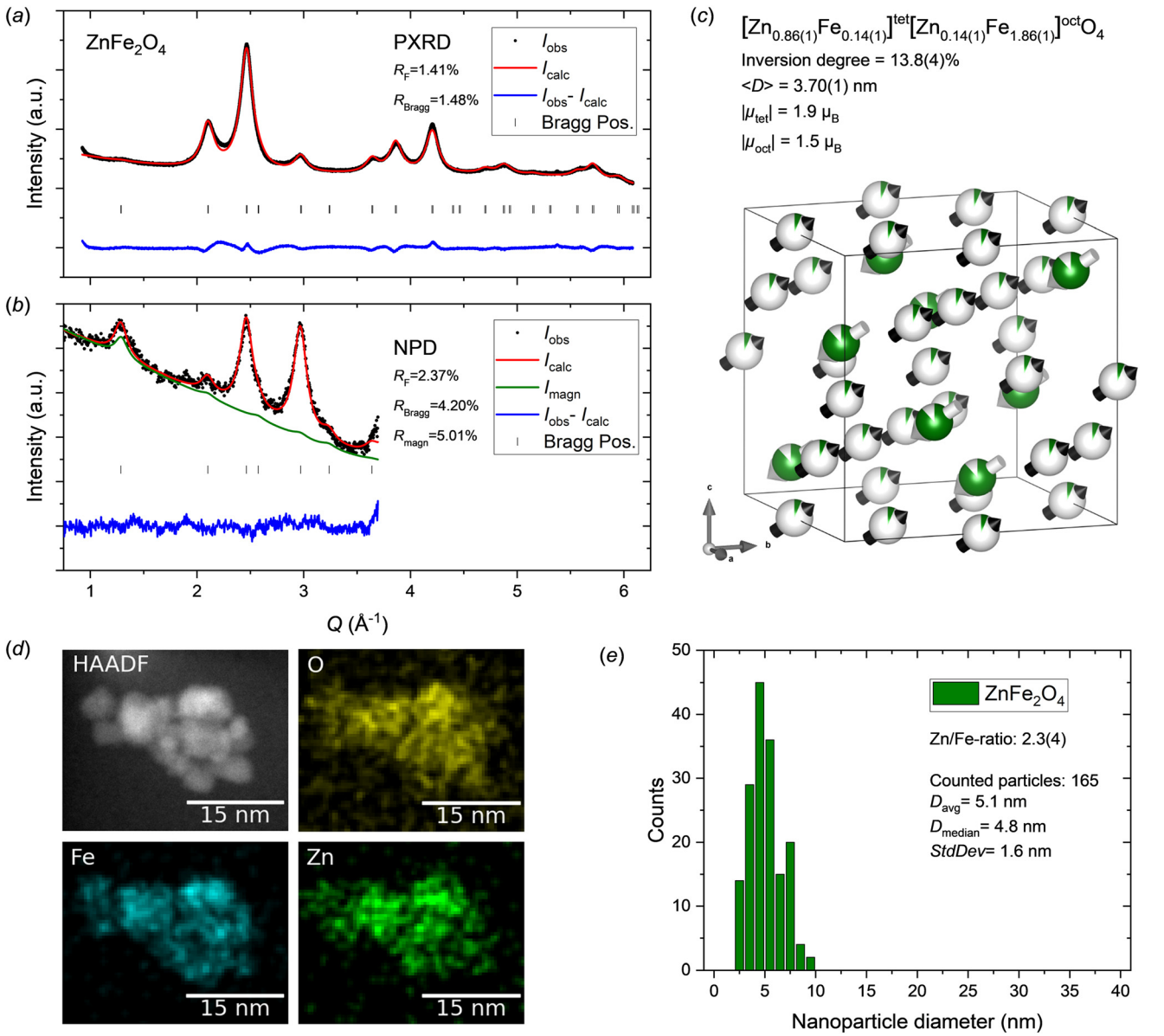

Fig. 5 a) PXRD and b) NPD data for $ZnFe_2O_4$ nanocrystallites with jointly refined Rietveld fits. c) Illustration of the refined crystal and magnetic structure of the $ZnFe_2O_4$ sample. The refined magnetic moment components on tetrahedral and octahedral sites are too small to be illustrated. The refined atomic site occupation fractions of Zn^{2+} (green) and Fe^{3+} (white) are illustrated on the spheres. The displayed arrows have been scaled ×2 compared to the other structural illustrations to make them visible. Illustration made with VESTA.[26] d) STEM-HAADF image and EDS elemental maps for the $ZnFe_2O_4$ nanoparticle sample. e) $ZnFe_2O_4$ nanoparticle size analysis from STEM data.

present study, all precursors were equivalently prepared by the NH_4OH method described earlier, and treated at identical physical reaction conditions, *i.e.* in an autoclave reactor at 200 °C for 1 h. However, in the previous studies various adjustments to the procedure were done, as indicated for the specific cases below, to promote certain product characteristics. The stronger NaOH base is often used as the precipitating agent in hydrothermal spinel ferrite synthesis, however, the NH_4OH precursor preparation route was used for the preparation of $MnFe_2O_4$ nanocrystallites in both this and our previous study. This is because the NaOH route does not yield phase pure $MnFe_2O_4$ samples, but instead leads to formation of a considerable amount of α-Fe_2O_3 impurity. Here, a higher synthesis temperature of 200 °C was used, which is found to cause formation of larger $MnFe_2O_4$ crystallites of 17.13(2) nm compared to 13.5(2) nm obtained at 150 °C. In addition, the higher temperature yields a higher inversion degree of 0.87(3) compared to the 0.643(3) obtained at 150 °C. A small increase in M_s is also observed. Since Mn^{2+} and Fe^{3+} ions have identical ground state $3d^5$ electron configurations, the increased M_s is likely a result of the larger crystallite size.

For $CoFe_2O_4$, the NaOH precursor route was used in two previous studies with different base concentrations of 12 M

Table 4 Atomic structure parameters for the $ZnFe_2O_4$ nanocrystallite sample

$ZnFe_2O_4$							
Space group: $Fd\bar{3}m$ (#227)							
Unit cell: $a = b = c = 8.4588(4)$ Å, $\alpha = b = \gamma = 90°$							
Fit quality PXRD: $R_{Bragg} = 1.48\%$, $R_F = 1.41\%$							
Fit quality NPD: $R_{Bragg} = 4.20\%$, $R_F = 2.37\%$, $R_{magn} = 5.01\%$							
Atom	Wyckoff site	x	y	z	B_{iso} (Å^2)	sof^a	$R_x{}^b$ (μ_B)
Zn	8*a*	0.125	0.125	0.125	0.51(2)^c	0.862(4)^d	0
Fe	8*a*	0.125	0.125	0.125	0.51(2)^c	0.138(4)^d	−8.1
Zn	16*d*	0.5	0.5	0.5	0.51(2)^c	0.069(2)^d	0
Fe	16*d*	0.5	0.5	0.5	0.51(2)^c	0.931(2)^d	0.9
O	32*e*	0.2489(3)	0.2489(3)	0.2489(3)	0.51(2)^c	1	0

Note: the numbers in parentheses indicate the errors on the last significant digit of the refined parameters. [a] Site occupation fraction (*sof*). [b] The magnetic moment vector component ($R_x = R_y = R_z$) refined along the ⟨111⟩ direction. [c] The atomic displacement parameters (B_{iso}) were constrained to be equal. [d] Linear restraints were imposed on the tetrahedral (8*a*) and octahedral (16*d*) site occupancies to avoid unphysical over-population and constrain to nominal composition.

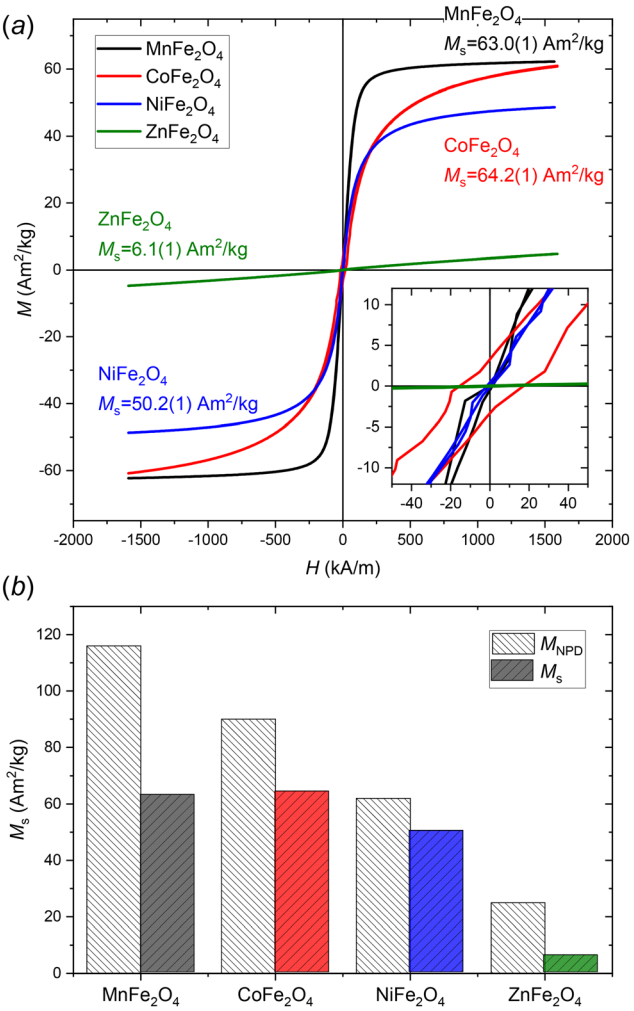

Fig. 6 a) Room temperature field dependent magnetisation curves of the $MnFe_2O_4$, $CoFe_2O_4$, $NiFe_2O_4$, and $ZnFe_2O_4$ nanoparticles with saturation magnetisations, M_s, (determined by law of approach to saturation) indicated. b) Comparison of intrinsic magnetizations estimated from the magnetic structure refinement of the NPD data (M_{NPD}) and the macroscopic saturation magnetizations from the VSM data (M_s).

and 16 M, respectively. The syntheses were carried out with identical physical reaction conditions in Study 1 (200 °C for 1 h) and at higher temperature and for longer time in Study 2 (240 °C for 2 h). The NH_4OH route yields much smaller crystallites of 7.92(1) nm compared to the 13.4(1) nm obtained using the 12 M NaOH route at identical synthesis conditions (200 °C, 1 h) and 17.6(1) nm using the stronger 16 M NaOH route for longer time and at higher temperature (240 °C, 2 h). This is consistent with observations in a previous *in situ* PXRD study of hydrothermal $CoFe_2O_4$ nanoparticle formation, where changing precursor pH or precursor concentration at the time of adding the precipitating base, proved to be a more efficient handle for changing particle sizes compared to varying synthesis temperature.[69] In the bulk, $CoFe_2O_4$ adopts a fully inverse spinel structure, *i.e.* Co^{2+} occupying half the octahedral sites. However, our structural studies of hydrothermally synthesised $CoFe_2O_4$ nanocrystallites consistently indicate that metastable mixed spinel cation configurations are obtained.[15,29] Interestingly, the smaller crystallites from the NH_4OH route exhibit a higher inversion degree of 0.954(6), which is closer to the thermodynamically stable fully inverse structure of the bulk compound, compared to the almost random/disordered distribution of 0.660(6) and 0.72(1) from the NaOH routes. Using a softer base may thus be less likely to induce formation of metastable cation configurations. The $CoFe_2O_4$ nanoparticles prepared through the NH_4OH route yield a lower M_s of 64.2(1) Am^2 kg^{-1} compared to the 71.7(2) and 74.0(2) Am^2 kg^{-1} produced by the NaOH routes. The M_s drop can be attributed to the higher inversion degree (*i.e.* a larger amount of the less magnetic $3d^7$ Co^{2+} ions replacing $3d^5$ Fe^{3+} on the octahedral site) along with the smaller crystallite size.

In the case of $NiFe_2O_4$, identical physical reaction conditions (*i.e.* autoclave reactor at 200 °C for 1 h) were used for the two different precursors of the present and previous study. As for $CoFe_2O_4$, a considerable difference in the obtained crystallite sizes is observed, with the NH_4OH

Table 5 Summary of hydrothermally synthesized spinel ferrite nanoparticle characteristics obtained in the present study compared to our previous studies employing different precursor routes and/or synthesis conditions

Compound	Study	Base type	Synthesis conditions	Crystallite size (nm)	Unit cell length (Å)	Inversion deg.	M_s (Am^2 kg^{-1})
$MnFe_2O_4$	This study	25% NH_4OH (pH = 10)	AC, 200 °C, 1 h	17.13(2)	8.49637(9)	0.87(3)	63.0(1)
	Study 1 (ref. 15)	25% NH_4OH (pH = 10)	AC, 150 °C, 1 h	13.5(2)[a]	8.46(12)	0.643(3)	60.5(1)
$CoFe_2O_4$	This study	25% NH_4OH (pH = 10)	AC, 200 °C, 1 h	7.92(1)	8.3901(1)	0.954(6)	64.2(1)
	Study 1 (ref. 15)	12 M NaOH (pH > 14)	AC, 200 °C, 1 h	13.4(1)	8.4018(1)[a]	0.660(6)	71.7(2)
	Study 2 (ref. 29)	16 M NaOH (pH > 14)	AC, 240 °C, 2 h	17.6(1)	8.3897(2)	0.72(1)	74.0(2)
$NiFe_2O_4$	This study	25% NH_4OH	AC, 200 °C, 1 h	10.31(1)	8.3574(1)	1	50.2(1)
	Study 1 (ref. 15)	12 M NaOH (pH > 14)	AC, 200 °C, 1 h	23.7(17)[a]	8.36(12)[a]	1	47.1(1)
$ZnFe_2O_4$	This study	25% NH_4OH	AC, 200 °C, 1 h	3.70(1)	8.4588(4)	0.138(4)	6.1(1)
	Study 1 (ref. 15)	12 M NaOH (pH > 14)	Flow (250 bar), 390 °C	9.8(1)	8.4376(3)	0.166(10)	10.8(1)
	Study 2 (ref. 29)	16 M NaOH (pH > 14)	AC, 240 °C, 2 h	11.0(1)	8.4515(2)	0.24(1)	20.5(1)

[a] Weighted average from bimodal size model.

precursor route yielding smaller 10.31(1) nm $NiFe_2O_4$ crystallites compared to 23.7(17) nm from the NaOH route. As in our previous studies using the NaOH route, refining the cation occupancies in the modelling of the diffraction data led to unphysical excess occupation by Ni on the octahedral site indicating a fully inverse structure.[15,68] Consequently, $NiFe_2O_4$ seemingly has a very strong affinity for the fully inverse spinel structure even for small crystallites of ~10 nm. Interestingly, despite the smaller crystallite size, a slightly larger M_s of 50.2(1) Am^2 kg^{-1} is obtained for the NH_4OH synthesized particles compared to 47.1(1) Am^2 kg^{-1} for the larger particles from the NaOH synthesis.

For $ZnFe_2O_4$, our two previous studies both used the NaOH precursor preparation route. In one case, 12 M NaOH was employed and the synthesis was carried out under supercritical hydrothermal conditions (390 °C, 250 bar) in a continuous flow reactor.[15,70] In the other case, the precursor preparation was done using a stronger 16 M NaOH solution and the synthesis carried out in an autoclave reactor at 240 °C for 2 h.[29] Here, the combination of using a softer NH_4OH base in the precursor preparation and carrying out the synthesis at a lower reaction temperature of 200 °C yields very fine $ZnFe_2O_4$ crystallites with an average diameter of 3.70(1) nm. For the NaOH studies, larger crystallites of 9.8(1) and 11.0(1) nm were obtained. In the bulk, $ZnFe_2O_4$ adopts a normal spinel structure, *i.e.* with Zn^{2+} exclusively occupying the tetrahedral site. However, for the nanosized crystallites a metastable mixed spinel configuration is consistently obtained. As for the $CoFe_2O_4$ samples, it seems that using a softer base causes a more bulk-like cation configuration with an inversion degree of 0.138(4) compared to the 0.24(1) obtained from the 16 M NaOH route. Since Zn^{2+} ions ($3d^{10}$ electron configuration) are non-magnetic, bulk $ZnFe_2O_4$ in the thermodynamically stable normal spinel configuration adopts an antiferromagnetic structure with a Néel temperature, T_N, of 10 K, *i.e.* paramagnetic at room temperature.[28,66] However, deviations from the normal spinel configuration undoes the perfect cancellation of the antiparallel $3d^5$ Fe^{3+} magnetic moments on the octahedral sites. Consequently, the nanocrystallites from our previous studies, with a higher degree of cation disorder, exhibit a higher saturation magnetisation than the crystallites with a more "normal" cation configuration.

Conclusion

The crystal and magnetic structures of hydrothermally synthesized $MnFe_2O_4$, $CoFe_2O_4$, $NiFe_2O_4$ and $ZnFe_2O_4$ nanocrystallites have been examined using joint structural modelling of PXRD and NPD data. By using weak 25% NH_4OH as the precipitating base in the precursor preparations it was possible to prepare phase-pure $MnFe_2O_4$, $CoFe_2O_4$, $NiFe_2O_4$ and $ZnFe_2O_4$ nanocrystallites employing identical hydrothermal synthesis conditions. This, in turn, allowed us to isolate and study the effect of the individual divalent ions on the obtained crystallite size and structure. The data reveals a substantial effect of the type of cation on the resulting nanocrystallite size, spinel cation configurations and magnetic structure/properties. The study highlights how a detailed fundamental understanding of the synthesis-structure–property relationship is essential for accurately predicting, designing, and tailoring spinel ferrite materials with specific or optimized properties.

Data availability

The data supporting this article are included in the article and ESI.†

Conflicts of interest

The authors declare no competing financial interests.

Acknowledgements

The authors are grateful for the obtained beamtime at the Cold Neutron Powder Diffractometer (DMC) instrument at the Swiss Spallation Neutron Source (SINQ), Paul Scherrer Institute (PSI), Villigen, Switzerland. Lukas Keller and Emmanuel Canévet are thanked for their support during the beamtime. This work was financially supported by the

Danish National Research Foundation (Center for Materials Crystallography, DNRF93), Innovation Fund Denmark (Green Chemistry for Advanced Materials, GCAM-4107-00008B), Independent Research Fund Denmark (Small and Smart Magnet Design), Danish Center for Synchrotron and Neutron Science (DanScatt), and Comunidad de Madrid, Spain, through an "Atracción de Talento Investigador" fellowship (2020-T2/IND-20581). C. G.-M. acknowledges financial support from grant RYC2021–031181-I funded by MCIN/AEI/10.13039/501100011033 and by the "European Union NextGenerationEU/PRTR". This project has received funding from the European Union's Horizon Europe research and innovation programme under grant agreement No 101063369 (OXYPOW) and No 101109595 (MAGWIRE). Affiliation with the Center for Integrated Materials Research (iMAT) at Aarhus University is gratefully acknowledged. EDB and RK acknowledge funding from the Carlsberg Foundation (CF18-0705), Aarhus University Centre for Integrated Materials Research and the Interdisciplinary Nanoscience Center.

References

1 J. M. D. Coey, *J. Magn. Magn. Mater.*, 2002, **248**, 441–456.
2 Q. Song and Z. J. Zhang, *J. Am. Chem. Soc.*, 2012, **134**, 10182–10190.
3 A. Quesada, C. Granados-Miralles, A. Lopez-Ortega, S. Erokhin, E. Lottini, J. Pedrosa, A. Bollero, A. M. Aragon, F. Rubio-Marcos, M. Stingaciu, G. Bertoni, C. D. J. Fernandez, C. Sangregorio, J. F. Fernandez, D. Berkov and M. Christensen, *Adv. Electron. Mater.*, 2016, **2**, 1500365.
4 Q. A. Pankhurst, J. Connolly, S. K. Jones and J. Dobson, *J. Phys. D: Appl. Phys.*, 2003, **36**, R167–R181.
5 C. C. Berry and A. S. G. Curtis, *J. Phys. D: Appl. Phys.*, 2003, **36**, R198–R206.
6 M. de h-Óra, A. Nicolenco, P. Monalisha, T. Maity, B. Zhu, S. Lee, Z. Sun, J. Sort and J. MacManus-Driscoll, *APL Mater.*, 2023, **11**, 051105.
7 Y. Yang, Z. Xi, Y. Dong, C. Zheng, H. Hu, X. Li, Z. Jiang, W.-C. Lu, D. Wu and Z. Wen, *ACS Appl. Mater. Interfaces*, 2020, **12**, 56300–56309.
8 D. Guin, B. Baruwati and S. V. Manorama, *Org. Lett.*, 2007, **9**, 1419–1421.
9 R. Abu-Reziq, H. Alper, D. S. Wang and M. L. Post, *J. Am. Chem. Soc.*, 2006, **128**, 5279–5282.
10 J. H. Lee, Y. M. Huh, Y. Jun, J. Seo, J. Jang, H. T. Song, S. Kim, E. J. Cho, H. G. Yoon, J. S. Suh and J. Cheon, *Nat. Med.*, 2007, **13**, 95–99.
11 H. B. Na, I. C. Song and T. Hyeon, *Adv. Mater.*, 2009, **21**, 2133–2148.
12 J. T. Jang, H. Nah, J. H. Lee, S. H. Moon, M. G. Kim and J. Cheon, *Angew. Chem., Int. Ed.*, 2009, **48**, 1234–1238.
13 C. A. Quinto, P. Mohindra, S. Tong and G. Bao, *Nanoscale*, 2015, **7**, 12728–12736.
14 A. H. Lu, E. L. Salabas and F. Schuth, *Angew. Chem., Int. Ed.*, 2007, **46**, 1222–1244.
15 H. L. Andersen, M. Saura-Múzquiz, C. Granados-Miralles, E. Canévet, N. Lock and M. Christensen, *Nanoscale*, 2018, **10**, 14902–14914.
16 K. R. Sanchez-Lievanos, J. L. Stair and K. E. Knowles, *Inorg. Chem.*, 2021, **60**, 4291–4305.
17 S. S. Chikazumi and C. D. Graham, *Physics of ferromagnetism*, Oxford University Press, Oxford, New York, 2nd edn, 2009.
18 E. Solano, C. Frontera, T. Puig, X. Obradors, S. Ricart and J. Ros, *J. Appl. Crystallogr.*, 2014, **47**, 414–420.
19 C. Liu, B. S. Zou, A. J. Rondinone and Z. J. Zhang, *J. Phys. Chem. B*, 2000, **104**, 1141–1145.
20 J. Jacob and M. A. Khadar, *J. Appl. Phys.*, 2010, **107**, 114310.
21 S. M. Patange, S. E. Shirsath, G. S. Jangam, K. S. Lohar, S. S. Jadhav and K. M. Jadhav, *J. Appl. Phys.*, 2011, **109**, 053909.
22 Z. Z. Lazarevic, C. Jovalekic, A. Milutinovic, D. Sekulic, V. N. Ivanovski, A. Recnik, B. Cekic and N. Z. Romcevic, *J. Appl. Phys.*, 2013, **113**, 187221.
23 T. Slatineanu, A. R. Iordan, M. N. Palamaru, O. F. Caltun, V. Gafton and L. Leontie, *Mater. Res. Bull.*, 2011, **46**, 1455–1460.
24 V. Blanco-Gutierrez, E. Climent-Pascual, M. J. Torralvo-Fernandez, R. Saez-Puche and M. T. Fernandez-Diaz, *J. Solid State Chem.*, 2011, **184**, 1608–1613.
25 Á. Gallo-Cordova, A. Espinosa, A. Serrano, L. Gutiérrez, N. Menéndez, M. del Puerto Morales and E. Mazarío, *Mater. Chem. Front.*, 2020, **4**, 3063–3073.
26 K. Momma and F. Izumi, *J. Appl. Crystallogr.*, 2011, **44**, 1272–1276.
27 J. M. D. Coey, *Magnetism and magnetic materials*, Cambridge University Press, Cambridge, 2010.
28 R. Skomski, *J. Phys.: Condens. Matter*, 2003, **15**, R841–R896.
29 H. L. Andersen, C. Granados-Miralles, M. Saura-Múzquiz, M. Stingaciu, J. Larsen, F. Søndergaard-Pedersen, J. V. Ahlburg, L. Keller, C. Frandsen and M. Christensen, *Mater. Chem. Front.*, 2019, **3**, 668–679.
30 B. Xavier and L. Amílcar, *J. Phys. D: Appl. Phys.*, 2002, **35**, 201.
31 S. Linderoth, P. V. Hendriksen, F. Bødker, S. Wells, K. Davies, S. W. Charles and S. Mørup, *J. Appl. Phys.*, 1994, **75**, 6583–6585.
32 B. Zhang, G. Tang, Z. Yan, Z. Wang, Q. Yang and J. Cui, *J. Wuhan Univ. Technol., Mater. Sci. Ed.*, 2007, **22**, 514–517.
33 W. Clegg, *Crystal structure analysis: principles and practice*, International Union of Crystallography; Oxford University Press, Chester, England, New York, 2001.
34 Z. Wang, X. Guo, J. Montoya and J. K. Nørskov, *npj Comput. Mater.*, 2020, **6**, 160.
35 J. B. Gerken, J. G. McAlpin, J. Y. C. Chen, M. L. Rigsby, W. H. Casey, R. D. Britt and S. S. Stahl, *J. Am. Chem. Soc.*, 2011, **133**, 14431–14442.
36 W. Sun, D. A. Kitchaev, D. Kramer and G. Ceder, *Nat. Commun.*, 2019, **10**, 573.
37 J. Schefer, P. Fischer, H. Heer, A. Isacson, M. Koch and R. Thut, *Nucl. Instrum. Methods Phys. Res., Sect. A*, 1990, **288**, 477–485.
38 J. Rodriguez-Carvajal, *Phys. B*, 1993, **192**, 55–69.

39 P. Thompson, D. E. Cox and J. B. Hastings, *J. Appl. Crystallogr.*, 1987, **20**, 79–83.
40 P. Scherrer, Nachrichten von der Gesellschaft der Wissenschaften zu Göttingen, *Mathematisch-Physikalische Klasse*, 1918, vol. 1918, pp. 98–100.
41 J. I. Langford and A. J. C. Wilson, *J. Appl. Crystallogr.*, 1978, **11**, 102–113.
42 G. Shirane, *Acta Crystallogr.*, 1959, **12**, 282–285.
43 J. Schindelin, I. Arganda-Carreras, E. Frise, V. Kaynig, M. Longair, T. Pietzsch, S. Preibisch, C. Rueden, S. Saalfeld and B. Schmid, *Nat. Methods*, 2012, **9**, 676–682.
44 F. de la Peña, E. Prestat, V. T. Fauske, P. Burdet, J. Lähnemann, P. Jokubauskas, T. Furnival, M. Nord, T. Ostasevicius, K. E. MacArthur, D. N. Johnstone, M. Sarahan, J. Taillon, T. Aarholt, V. Migunov, A. Eljarrat, J. Caron, C. Francis, T. Nemoto, T. Poon, S. Mazzucco, N. Tappy, N. Cautaerts, S. Somnath, T. Slater, M. Walls, F. Winkler and H. W. Ånes, *hyperspy/hyperspy: Release v1.7.3 (v1.7.3)*, Zenodo, 2022, DOI: **10.5281/zenodo.7263263**.
45 Pandas-developement-team.
46 C. R. Harris, K. J. Millman, S. J. van der Walt, R. Gommers, P. Virtanen, D. Cournapeau, E. Wieser, J. Taylor, S. Berg, N. J. Smith, R. Kern, M. Picus, S. Hoyer, M. H. van Kerkwijk, M. Brett, A. Haldane, J. F. Del Rio, M. Wiebe, P. Peterson, P. Gerard-Marchant, K. Sheppard, T. Reddy, W. Weckesser, H. Abbasi, C. Gohlke and T. E. Oliphant, *Nature*, 2020, **585**, 357–362.
47 J. D. Hunter, *Comput. Sci. Eng.*, 2007, **9**, 90–95.
48 P. Virtanen, R. Gommers, T. E. Oliphant, M. Haberland, T. Reddy, D. Cournapeau, E. Burovski, P. Peterson, W. Weckesser, J. Bright, S. J. van der Walt, M. Brett, J. Wilson, K. J. Millman, N. Mayorov, A. R. J. Nelson, E. Jones, R. Kern, E. Larson, C. Carey, İ. Polat, Y. Feng, E. W. Moore, J. VanderPlas, D. Laxalde, J. Perktold, R. Cimrman, I. Henriksen, E. A. Quintero, C. R. Harris, A. M. Archibald, A. H. Ribeiro, F. Pedregosa and P. van Mulbregt, SciPy 1.0 Contributors, *Nat. Methods*, 2020, **17**, 261–272.
49 V. Valvoda, *International Tables for Crystallography, Volume C: Mathematical, Physical and Chemical Tables*, Kluwer Acedemic Publishers, Dordrecht/Boston/London, 3rd edn, 2004, ch. 4.
50 A. J. Blake and W. Clegg, *Crystal structure analysis: principles and practice*, Oxford University Press, Oxford, New York, 2nd edn, 2009.
51 H. L. Andersen, B. A. Frandsen, H. P. Gunnlaugsson, M. R. V. Jorgensen, S. J. L. Billinge, K. M. O. Jensen and M. Christensen, *IUCrJ*, 2021, **8**, 33–45.
52 B. Antic, A. Kremenović, A. S. Nikolic and M. Stoiljkovic, *J. Phys. Chem. B*, 2004, **108**, 12646–12651.
53 C. Wende, K. Olimov, H. Modrow, F. E. Wagner and H. Langbein, *Mater. Res. Bull.*, 2006, **41**, 1530–1542.
54 M. E. Fleet, *J. Solid State Chem.*, 1986, **62**, 75–82.
55 J. E. Jørgensen, L. Mosegaard, L. E. Thomsen, T. R. Jensen and J. C. Hanson, *J. Solid State Chem.*, 2007, **180**, 180–185.
56 R. Nepal, M. Saghayezhian, J. Zhang and R. Jin, *J. Magn. Magn. Mater.*, 2020, **497**, 165955.
57 J. M. Hastings and L. M. Corliss, *Phys. Rev.*, 1956, **104**, 328–331.
58 S. Yanez-Vilar, M. Sanchez-Andujar, C. Gomez-Aguirre, J. Mira, M. A. Senaris-Rodriguez and S. Castro-Garcia, *J. Solid State Chem.*, 2009, **182**, 2685–2690.
59 C. Liu, A. J. Rondinone and Z. J. Zhang, *Pure Appl. Chem.*, 2000, **72**, 37–45.
60 R. Borah and S. Ravi, *J. Magn. Magn. Mater.*, 2021, **538**, 168276.
61 Z. Li, J. Dai, D. Huang and X. Wen, *J. Alloys Compd.*, 2022, **907**, 164386.
62 I. H. Gul and E. Pervaiz, *Mater. Res. Bull.*, 2012, **47**, 1353–1361.
63 K. Raju and D. H. Yoon, *J. Supercond. Novel Magn.*, 2014, **27**, 1285–1292.
64 R. Kalia, R. Pushpendra, R. K. Kunchala, S. N. Achary and B. S. Naidu, *J. Alloys Compd.*, 2021, **875**, 159905.
65 N. Pailhé, A. Wattiaux, M. Gaudon and A. Demourgues, *J. Solid State Chem.*, 2008, **181**, 1040–1047.
66 A. Kremenovic, B. Antic, P. Vulic, J. Blanusa and A. Tomic, *J. Magn. Magn. Mater.*, 2017, **426**, 264–266.
67 S. Blundell, *Magnetism in condensed matter*, Oxford University Press, Oxford; New York, 2001.
68 J. Hölscher, H. L. Andersen, M. Saura-Múzquiz, P. G. Garbus and M. Christensen, *CrystEngComm*, 2020, **22**, 515–524.
69 H. L. Andersen and M. Christensen, *Nanoscale*, 2015, **7**, 3481–3490.
70 P. Hald, J. Becker, M. Bremholm, J. S. Pedersen, J. Chevallier, S. B. Iversen and B. B. Iversen, *J. Solid State Chem.*, 2006, **179**, 2674–2680.